Supplementary Materials: Low–dimensional Models for Aerofoil Icing

David Massegur [1], Declan Clifford [1], Andrea Da Ronch [1,*], Riccardo Lombardi [2] and Marco Panzeri [2]

1. POD Model Convergence with Modes

The clustering technique provided large improvements in the rime ice region, that is, the region with the simpler and smoother shapes. It was found that for the global model, 20 POD modes were required to capture 95% of shape variance. Breaking this down into the clustering, the cluster corresponding to shapes with only 1 turning point resulted sufficiently described with just 2 POD modes. In terms of cluster corresponding to shapes with more than 1 turning point, however, we did not find significant change in the first singular value weightings on comparison with the unclassified data set. This is due to the cluster being composed of the more complex shape types. In that region, there is a wide variety of shape types, which makes it difficult for fewer POD modes to successfully reconstruct a shape. Forming subgroups according to specific shape types within this cluster could improve the local POD performance. However, doing this would require significantly more data points, all of which would need to be concentrated along narrow bands which align with a specific shape type.

2. NN+Conv-AE Architecture for Ice Profile Predictions

The final architecture of the two–step NN+Conv-AE adopted for the prediction of ice profiles is reported in Table S1.

3. NN+Conv-AE Architecture for Aero–icing Predictions

Table S2 reports the DNN architecture adopted for the prediction of the aero–icing characteristics.

4. Low–order Models Convergence with Number of Samples

This Section tells about the intermediate results we obtained when generating low–order models on subsequent iterations of the DOE samples. Whereas results presented in the main document employed the entire set of sample points, this Section reveals what we found as the set of sample points was increased. The iterations of the DOE are illustrated, with the results related to the last iterations being shown in the main document only.

4.1. Convergence for Predicting Ice Mass

The dependence of the predicted ice mass on the DOE iterations is illustrated in Figure S1 for the global POD model, in Figure S2 for the local POD model, and in Figure S3 for the convolutional autoencoder, respectively. For all low–order models, the region of higher LOOCV error stays confined along the isotherm, with the largest error not affected significantly by the increase in sample points. Implicitly, this reaffirms the utility of an adaptive strategy where additional samples are placed in regions of complex ice shapes. The history of the location of the largest ice mass is found to converge after the second iteration, reassuring the total number of sample points is adequate.

4.2. Convergence for Predicting Maximum Lift Coefficient

The history of the predicted maximum lift coefficient is summarised in Figure S4 for the global POD model, in Figure S5 for the local POD model, and in Figure S6 for the DNN model. Common to all the low–order models is the convergence of the results in terms of number of sample points. In this instance, both the rapid gradient towards the no–ice region and the moderate gradient found moving towards colder temperatures are unchanged after the second DOE iteration.

Table S1. NN+Conv-AE layer sizes used for the prediction of the ice profiles.

Layer	Dimension	Kernel	Stride	Padding
Encoder:				
Input	195×1			
Conv1D 1	91×13	$1 \times 13 \times 15 + 13$	1	7
AvgPool1D 1	-	15	2	0
Tanh				
Conv1D 2	39×19	$13 \times 19 \times 15 + 19$	1	7
AvgPool1D 2	-	15	2	0
Tanh				
Conv1D 3	13×26	$19 \times 26 \times 15 + 26$	1	7
AvgPool1D 3	-	15	2	0
Tanh				
Decoder:				
Latent	13×26			
TransConv1D 1	39×19	$26 \times 19 \times 15 + 19$	2	0
Tanh				
TransConv1D 2	91×13	$19 \times 13 \times 15 + 13$	2	0
Tanh				
TransConv1D 3	195×1	$13 \times 1 \times 15 + 1$	2	0
Input NN:				
Input	2			
Dense 1	56	$2 \times 56 + 56$		
Tanh				
Dense 2	112	$56 \times 112 + 112$		
Tanh				
Dense 3	169	$112 \times 169 + 169$		
Tanh				
Dense 4	338	$169 \times 338 + 338$		
Tanh				
Reshape	13×26			

Table S2. DNN layer sizes used for the global prediction of the aero–icing characteristics.

Layer	Size	Kernel
Input	2	
Dense 1	56	$2 \times 56 + 56$
Tanh		
Output	2	$56 \times 2 + 2$

4.3. Convergence History

A final outlook on the convergence history is shown in Figure S7. The average error, averaged over all the samples contained in the DOE population, is presented for the three quantities of interest: ice area, lift coefficient at stall, and stall angle of attack. Unanimously and monotonically, low–order models improve their accuracy. Smaller errors are achieved in all cases by the NN model, with the global POD model presenting the largest residual errors.

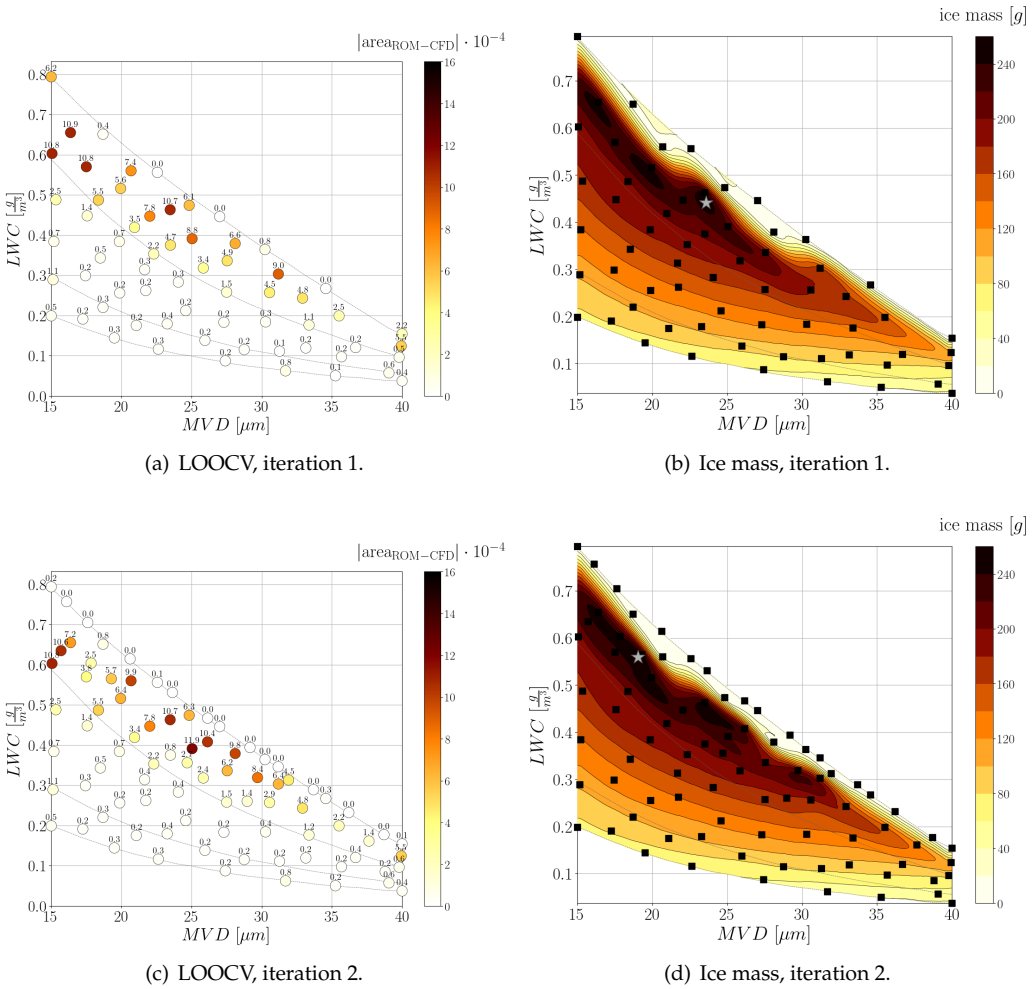

(a) LOOCV, iteration 1. (b) Ice mass, iteration 1.

(c) LOOCV, iteration 2. (d) Ice mass, iteration 2.

Figure S1. Convergence of global POD model for predicting ice mass. On the left, LOOCV of total ice area and on the right, ice mass.

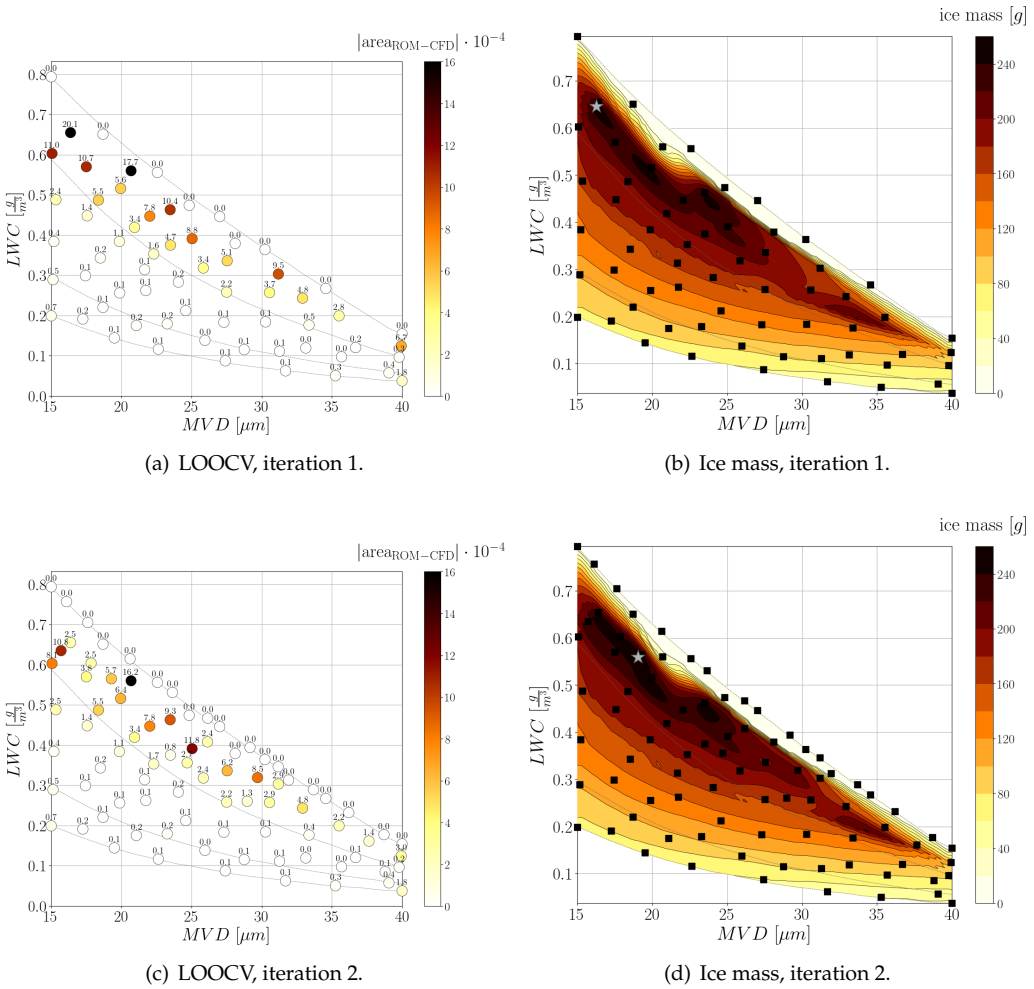

(a) LOOCV, iteration 1.

(b) Ice mass, iteration 1.

(c) LOOCV, iteration 2.

(d) Ice mass, iteration 2.

Figure S2. Convergence of local POD model for predicting ice mass. On the left, LOOCV of total ice area and on the right, ice mass.

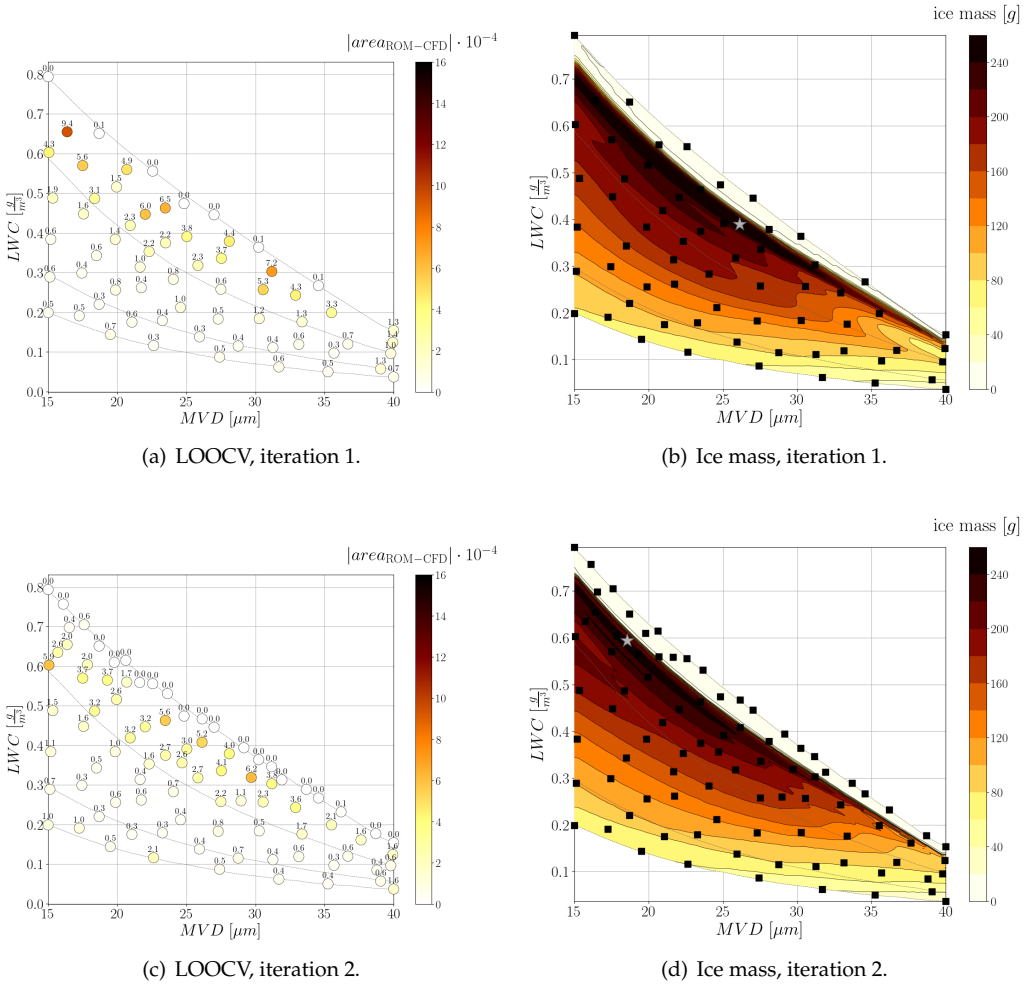

(a) LOOCV, iteration 1.

(b) Ice mass, iteration 1.

(c) LOOCV, iteration 2.

(d) Ice mass, iteration 2.

Figure S3. Convergence of global convolutional autoencoder for predicting ice mass. On the left, LOOCV of total ice area and on the right, ice mass.

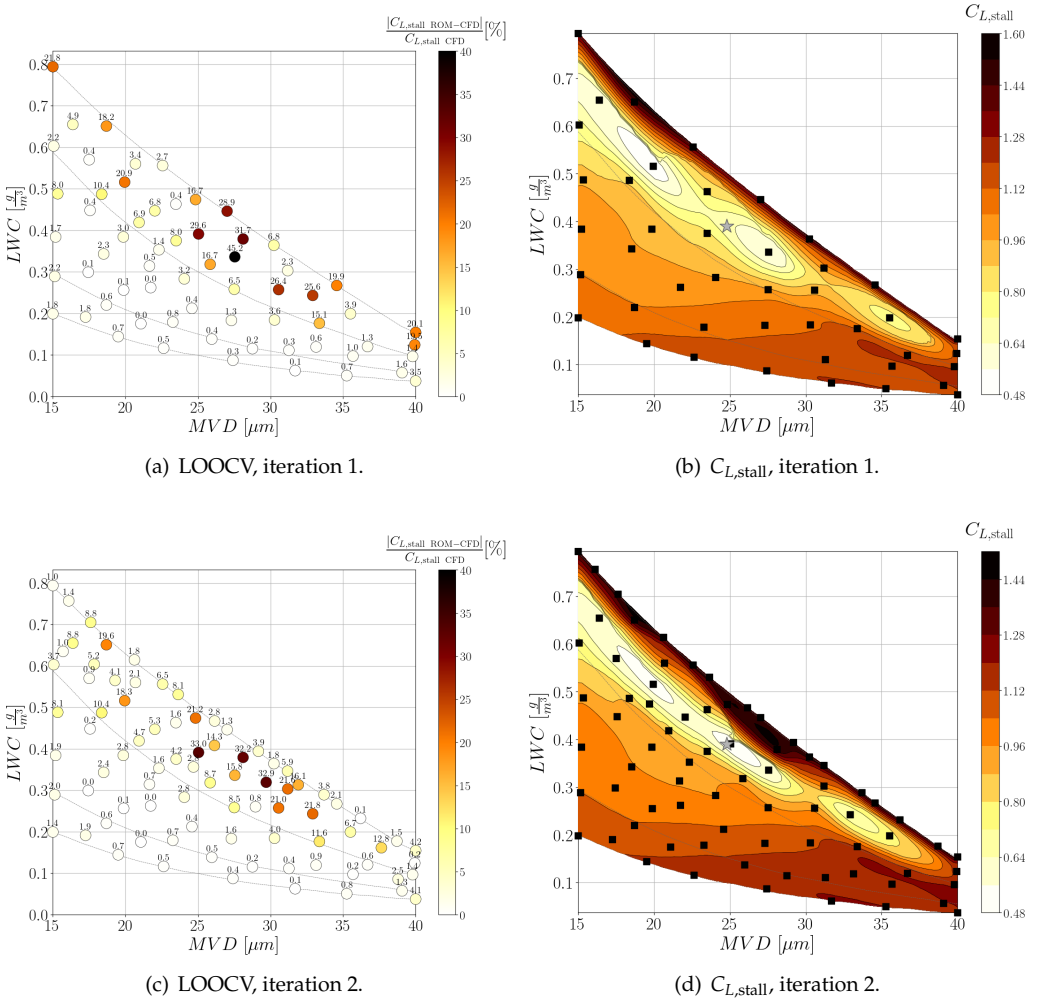

(a) LOOCV, iteration 1.

(b) $C_{L,\text{stall}}$, iteration 1.

(c) LOOCV, iteration 2.

(d) $C_{L,\text{stall}}$, iteration 2.

Figure S4. Convergence of global POD model for predicting maximum lift coefficient, $C_{L,\text{stall}}$. On the left, LOOCV of $C_{L,\text{stall}}$ and on the right, $C_{L,\text{stall}}$.

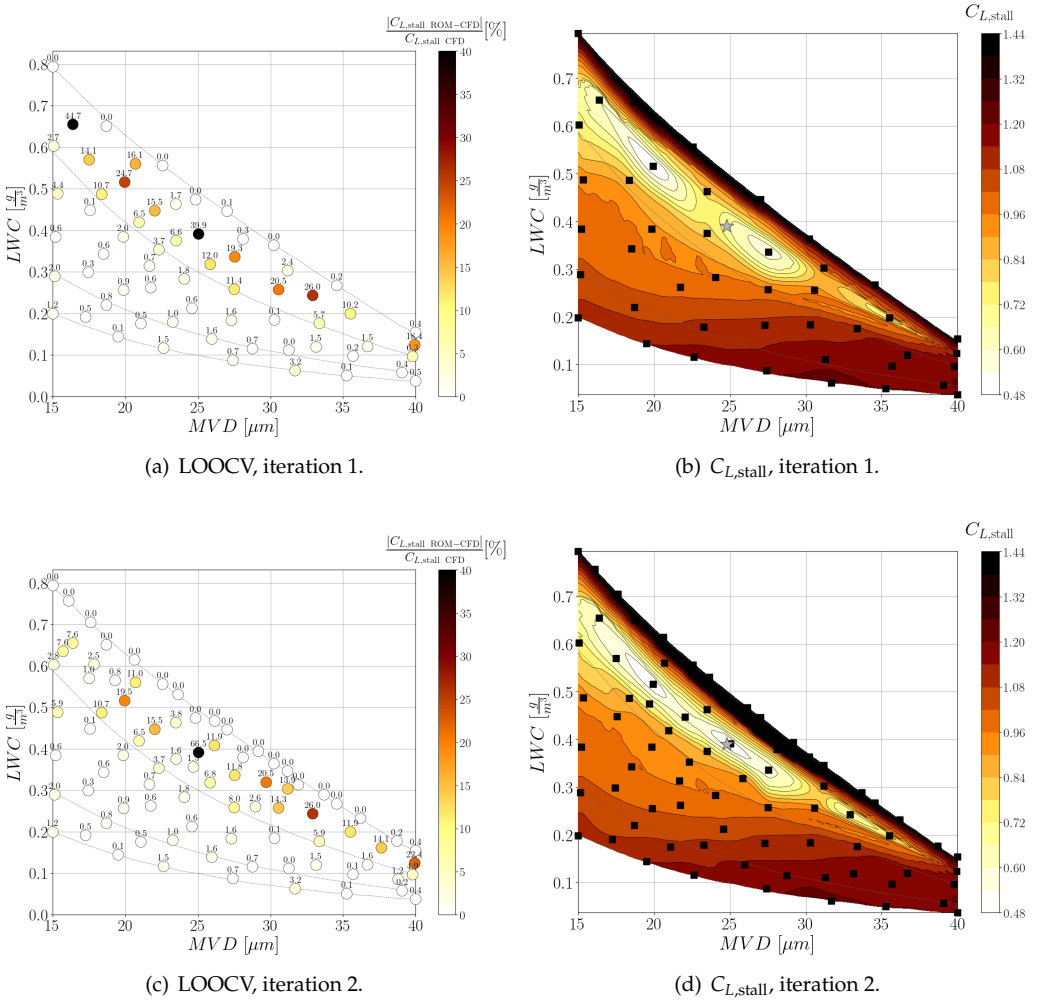

(a) LOOCV, iteration 1.

(b) $C_{L,\text{stall}}$, iteration 1.

(c) LOOCV, iteration 2.

(d) $C_{L,\text{stall}}$, iteration 2.

Figure S5. Convergence of local POD model for predicting maximum lift coefficient, $C_{L,\text{stall}}$. On the left, LOOCV of $C_{L,\text{stall}}$ and on the right, $C_{L,\text{stall}}$.

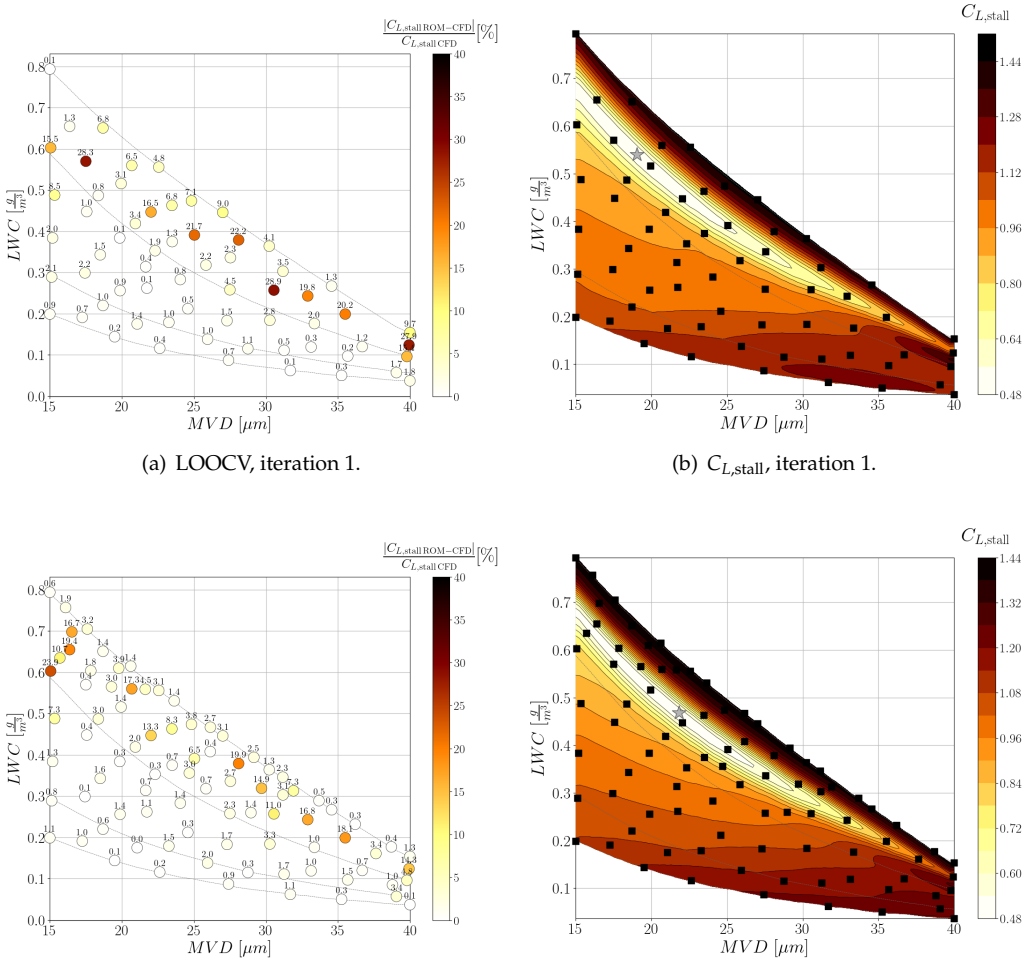

(a) LOOCV, iteration 1.

(b) $C_{L,\text{stall}}$, iteration 1.

(c) LOOCV, iteration 2.

(d) $C_{L,\text{stall}}$, iteration 2.

Figure S6. Convergence of global DNN for predicting maximum lift coefficient, $C_{L,\text{stall}}$. On the left, LOOCV of $C_{L,\text{stall}}$ and on the right, $C_{L,\text{stall}}$.

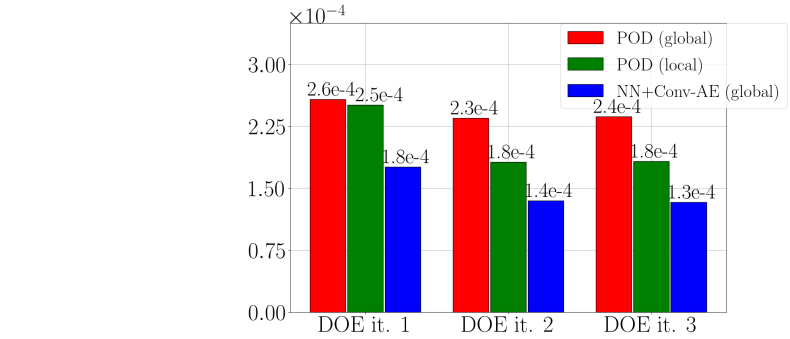

(a) Ice area.

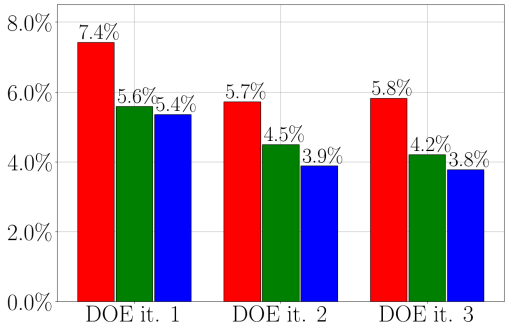

(b) $C_{L,\text{stall}}$.

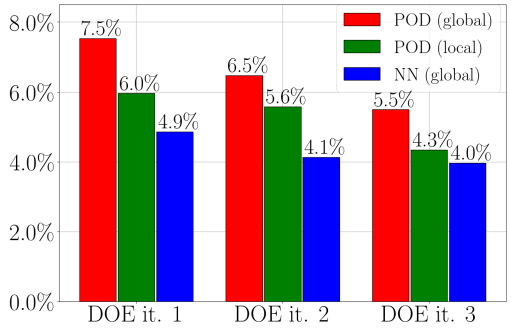

(c) α_{stall}.

Figure S7. History of LOOCV average errors for all low–order models through the DOE iterative sampling.